Oscillatory nature of the Okmok volcano's deformation

D. Walwer [*], M. Ghil [1], E. Calais

Geosciences Department, Ecole Normale Supérieure, PSL Research University, Paris, France

A B S T R A C T

The time-dependent deformation of volcanic edifices can help one understand the dynamics of pre-eruptive overpressure build-up in magma chambers. Thus, geodetic time series recorded at the Okmok volcano, in Alaska, show a pattern of fast and short inflations — referred to as "pulses" — followed by either slower and longer deflations, or time intervals with no deformation. This pattern is superimposed onto a longer-period inflation. A rapid inflation occurred just before the 2008 eruption, which suggests that the underlying process may lead to eruptions. It is crucial to understand whether such a behavior is driven by external forcing, such as melt supply variations, or whether it can develop spontaneously within the volcano's plumbing system. Here we model the observed oscillations (2004–2008) as resulting from the hydraulic interaction between two shallow magma chambers fed by a deeper source region, a geometry that is consistent with geochemical, petrological, and geophysical data. The model shows that episodes of periodic fast inflations occur (i) when a viscosity gradient is present in the vertical pipe, for instance as the result of a temperature gradient; and (ii) when the flux supplying the shallower chamber lies between two bounds that we derive analytically. The deformation pulses observed at Okmok can, therewith, be fully explained by the internal variability of the magmatic system and do not require time-variable external forcing. The proposed model can also be seen as an improvement upon the classic hydraulic models regularly used to explain a commonly observed pattern of volcanic deformations, i.e. exponential inflation.

© 2018 Elsevier B.V. All rights reserved.

1. Introduction

Volcanic eruptions are often considered to occur when the overpressure inside a shallow magma chamber is large enough for the tensile stress acting on the chamber's walls to exceed the tensile strength of the surrounding rock. The induced fracture can lead to a dyke filled with magma from the reservoir to propagate until it reaches the surface (e.g., Blake, 1981). Monitoring the evolution of overpressure in a magmatic reservoir is therefore key to understanding the mechanism behind the onset of eruptions. Deformation observations offer the opportunity to accomplish this task because the deformation of volcanic edifices is often directly related to magma chamber overpressure (e.g., Mogi, 1958; McTigue, 1987).

A common temporal pattern of deformation observed at volcanoes is that of exponential inflations and deflations (e.g. Dvorak and Okamura, 1987; Reverso et al., 2014). These phenomena can be explained by the linear dynamics of magma influx or outflux

driven by a pressure gradient between a storage reservoir embedded in an elastic medium, on the one hand, and a deeper source region or the surface, on the other (e.g. Jaupart and Tait, 1990; Lenglin et al., 2008; Pinel et al., 2010). In this case, the characteristic time scale of deflation is smaller than that of inflation, as shown for instance by time series of tilt measurements at the Kilauea volcano in Hawaii (Dvorak and Okamura, 1987).

Other types of temporal deformation patterns — such as the one reported by Walwer et al. (2016) and Ji et al. (2017) at Akutan, with its rapid inflation phases and slower deflations — are more difficult to relate to physical processes. This type of behavior is sometimes interpreted as the result of ad hoc time-dependent forcing mechanisms, be it "pulses" of magma flux, degassing or heat flux (e.g., Biggs et al., 2009, 2010; Peltier et al., 2009). Here we seek instead to understand this behavior as a manifestation of the magmatic system's internal variability. As we shall see, this approach allows us to understand the conditions under which the occurrence of such pulsating behavior is possible.

To do so, we take the Okmok volcano as a case study because of the relatively large geophysical, petrological, and geochemical dataset that is available, and of the associated long geodetic time series that show both gradual inflations and pulsating behavior with episodes of fast inflations (Biggs et al., 2010;
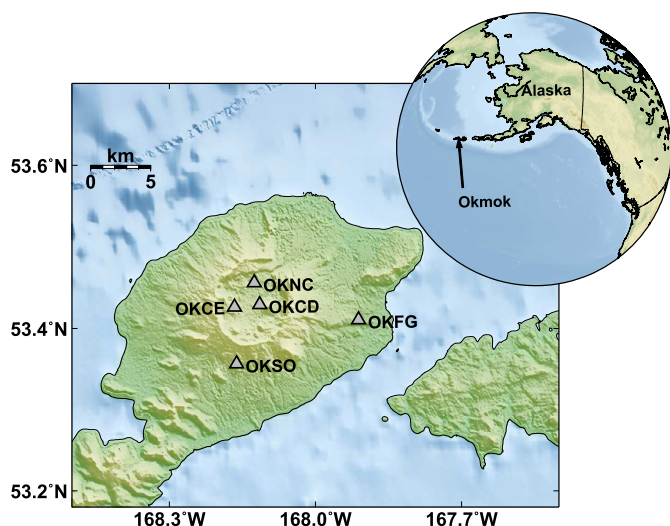
Fig. 1. Location map of the Okmok shield volcano, showing the GPS sites (grey triangles) from which the displacement time series used herein have been extracted.

Fig. 2. Geodetic time series related to the recent deformation history of Okmok volcano, 1997–2008. (a) Cumulative volume change estimated from InSAR time series, cf. Biggs et al. (2010). The error bars correspond to the uncertainties in the volume changes obtained by the inversion. The two vertical dashed lines represent, from left to right, the end of the 1997 eruption and the beginning of the 2008 eruption. The rectangular inset in panel (a) shows the time window presented in panel (b). (b) A selected GPS time series reflecting the deformation regime before the 2008 eruption. Note that the abscissa of panel (a) starts in 1996, while the one in panel (b) starts in 2003; both abscissas end in 2008.

Masterlark et al., 2010; Larsen et al., 2013). Caricchi et al. (2014) integrated this substantial dataset into a model in which surface deformation is driven by the thermodynamic evolution of phase equilibrium in a magma reservoir under the influence of crystallization, remelting, and degassing. Their model is consistent with a geodetic inversion suggesting that the deformation source remained stable from 1997 to 2008; because of its large number of degrees of freedom, though, does not provide a simple understanding of the conditions under which the observed deformation pulses can occur.

Here, instead, we rely on an approach that was previously proposed in the context of volcanology by Whitehead and Helfrich (1991) and Barmin et al. (2002). This approach relies on a model with a small number of variables that is mathematically quite tractable. We show that such a model provides a simple explanation for the circumstances under which the volcanic system can produce oscillatory pressure variations inside magma chambers, variations that can eventually result in deformation pulses like the observed ones.

2. Geophysical observations

The Okmok shield volcano (Fig. 1) is one of the most active of the Aleutian arc and it benefits from a set of geophysical and geochemical observations that suffices to infer its plumbing system and its deformation history. These two elements are crucial for our study, and they are briefly reviewed below.

2.1. Evidence for multiple reservoirs

Larsen et al. (2013) analyzed and compared samples from cones and vents created during Okmok's various eruptions in the last 1000–2000 yr. Their trace element compositions plotted against the SiO_2 weight fraction show two distinct poles: one with less than 53% SiO_2 weight fraction, while the other corresponds to a more evolved melt with SiO_2 larger than 53 wt.%. The two poles are separated by roughly 1 wt.% of SiO_2, as shown in Larsen et al. (2013, Fig. 4).

These authors interpret their geochemical data as evidence for shallow magma chambers in which melt evolved for about 2000 yrs and thus became enriched in silica, with more mafic melt inflow from a deeper reservoir, just before the 2008 eruption. This inference is consistent with observations that ascertain the more mafic character of the materials from eruptions that occurred
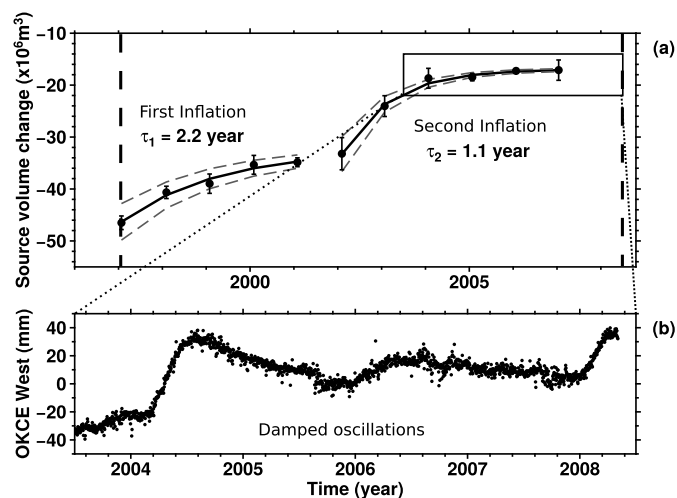
between 1900 and 1997, compared to the preceding ones, thus significantly breaking the long-term trend of silica enrichment.

The spatial pattern of deformation observed using GPS instrumentation shows that both the source of the precursory inflation that occurred in 2008, just before the eruption, and the source of the co-eruptive deflation are shallower and horizontally shifted from the source of the 1997 and 2008 deformation episodes (Freymueller and Kaufman, 2010). Freymueller and Kaufman (2010) also reported that the post-eruptive deformation corresponds to an uplift superimposed over a broader subsidence. This deformation pattern suggests that a shallow storage zone is inflating while a deeper one is deflating.

2.2. Geodetic time series, 1997–2008

The history of surface deformation between the end of the 1997 eruption and the beginning of the 2008, as derived from InSAR and GPS data, is plotted in Figs. 2(a, b). This history shows that the 1997 co-eruptive deflation was followed by an inflation; in Fig. 2, the inflations are reflected by the positive volume variations shown in the figure. The inflation rate exponentially decreases until becoming almost null by mid-2002; see also Lu et al. (2010) for the corresponding InSAR images. Then Okmok starts to inflate again at a progressively decreasing rate, until a new eruption that occurred in 2008.

These two inflation episodes have different time constants τ, which we estimate by fitting exponential functions to the InSAR-derived cumulative volume time series in Fig. 2a, namely $\tau_1 \simeq 2.2$ yr for the first episode, and $\tau_2 \simeq 1.1$ yr for the second one. The inflation rate during the second episode is thus decreasing faster than during the first one.

The higher temporal resolution and accuracy of GPS observations provides the additional observation of a change in the temporal deformation pattern before the 2008 eruption. From 2004 to 2008, GPS time series show two oscillation cycles superimposed onto the second exponential inflation phase mentioned above. They both start with a fast and relatively short inflation followed by a longer, almost flat, subsidence; see Fig. 2b here, and also Biggs et al. (2010, Fig. 7). The amplitude of the second oscillation is
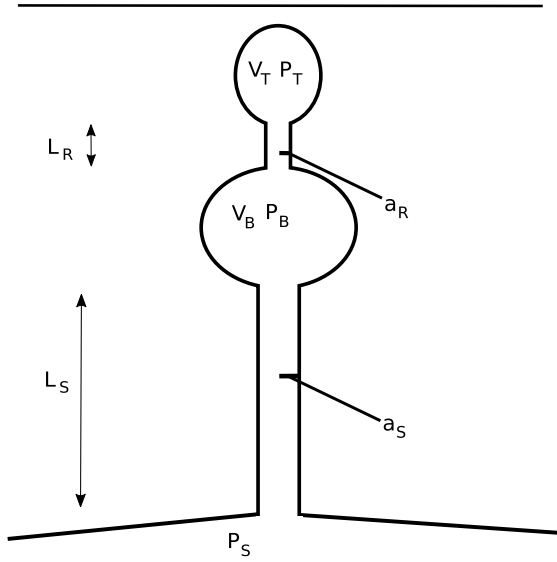
Fig. 3. Schematic representation of the components of the model described in the main text, including some of the associated parameters. Two shallow reservoirs with volumes V_B and V_T, respectively, contain magma at pressures P_B and P_T. They are fed by a deeper source region of constant pressure P_S. The pipe segments that link the deeper source to the lower chamber and the latter to the upper chamber have dimensions (a_S, L_S) and (a_R, L_R), respectively.

smaller than the first one, suggesting a damped oscillation regime. The last deflation of the second oscillation is followed by a fast precursory inflation, followed immediately by the co-eruptive subsidence that resulted from the 2008 eruption.

3. Model of magma reservoir interactions

3.1. Fluid flow in a pipe with temperature-dependent viscosity

Classical linear hydraulic interactions between magma reservoirs — as used for instance by Reverso et al. (2014) to explain the deformation episodes observed at Grímsvotn volcano in Iceland — cannot spontaneously give rise to oscillations or to the alternating fast and slow inflations and deflations observed at Okmok; see Appendix A. A limitation of this approach is that it does not account for viscosity variations in the melt, which must occur as temperature changes and/or fluid exsolution takes place as well as crystallization induced by either or both mechanisms (Blundy and Cashman, 2001).

We introduce, therefore, a model of fluid flow in a vertical cylindrical pipe along which a vertical temperature-driven viscosity gradient exists. We also discuss in Section 5.3 a model with viscosity change driven by crystallization induced by gas exsolution, and show there that both types of flow models can result in the same qualitative dynamics.

In our main model presented herewith, a pipe of length L_R and radius a_r connects two shallow chambers of volume V_T and V_B, and pressure P_T and P_B, respectively; the subscript, B and T refer to bottom and top. As the magma rises through the pipe, part of the advected heat is lost by diffusion through the pipe wall into the surrounding medium. The resulting decrease of temperature in the magma induces a viscosity increase described quantitatively below. The bottom chamber is connected to a source region inside which the pressure P_S is constant, supplying the shallow reservoirs with magma of constant viscosity through a pipe of radius a_S and length L_S. A schematic representation of the system is displayed in Fig. 3.

Our model of the flow in the cylindrical pipe connecting the shallow chambers builds upon the theory of Whitehead and Hel-

frich (1991), which is supported by experimental observations. We use a cylindrical system of coordinates, with r the radius and z the height. We take the z-axis to be oriented positively upwards and the reference level $z = 0$ is located at the basis of the pipe.

We assume that the flow is in a laminar regime and that the vertical velocity is the only nonzero component of the velocity field. We consider the horizontally averaged momentum equation in the vertical direction:

$$\frac{dw}{dt} = -\frac{1}{\rho}\frac{dP}{dz} - \rho g - \frac{8\nu(T)w}{a_R^2}; \tag{1}$$

here w is the horizontally averaged vertical velocity, P is the fluid pressure, ρ and g are the bulk density of the magma and the acceleration of gravity, $\nu(T)$ is the temperature-dependent kinematic viscosity, and a_R is the radius of the pipe, cf. Jaupart and Tait (1990).

The viscosity ν is assumed to depend linearly on temperature T, according to:

$$\nu(T) = \nu_B + \alpha(T_B - T), \tag{2}$$

where ν_B and T_B are reference values. We assume a steady-state regime for the temperature inside the cylindrical conduit, in which the vertical temperature advection is balanced by the radial temperature diffusion:

$$w\frac{\partial T}{\partial z} = \kappa \frac{1}{r}\frac{\partial}{\partial r}\left(r\frac{\partial T}{\partial r}\right). \tag{3}$$

The boundary condition for the partial differential equation (3) on the wall, at $r = a_R$, is

$$T = T_H - \frac{\Delta T}{L_R}z, \tag{4}$$

which yields, in particular, that $T = T_H$ at the basis of the pipe, where $z = 0$.

According to Eqs. (3) and (4), a vertical temperature gradient is always developing in the pipe and its surroundings as the magma is rising; see, for instance, Delaney and Pollard (1982), Bruce and Huppert (1989) and Jaupart and Mareschal (2010, p. 325). One easily verifies that

$$T = T_H - \frac{\Delta T}{L_R}z + \frac{w\Delta T}{4\kappa L_R a_R^2}(a_R^2 - r^2) \tag{5}$$

is a particular solution of equation (3). The homogeneous solution that has to be added to the particular one must have $T = T_H$ when $z = 0$.

For analytical convenience we follow Whitehead and Helfrich (1991) and approximate the temperature along the axis of the pipe, at $r = 0$, as follows:

$$T = T_H \quad \text{for} \quad 0 < z < \frac{wa_R^2}{4\kappa}, \quad \text{and}$$

$$T = T_H - \frac{\Delta T}{L_R}z + \frac{w\Delta T}{4\kappa L_R a_R^2} \quad \text{for} \quad \frac{wa_R^2}{4\kappa} < z < L. \tag{6}$$

This approximation is consistent with the boundary conditions, in particular with $T = T_H$ at $z = 0$. The length $L^* = wa_R^2/4\kappa$ equals the depth below which most of the heat that entered the conduit still resides in the fluid, resulting in a uniform temperature T_H (Delaney and Pollard, 1982).

Let us substitute solution (6) into the momentum equation (1) and integrate it from the bottom to the top of the conduit. This integration gives:

$$\frac{-1}{\rho}((P_B - P_T) + \rho g L_R)$$

$$= \begin{cases} \dfrac{8w}{a_R^2}\left[v_B L_R + \alpha\dfrac{\Delta T}{2L_R}\left(L_R - \dfrac{wa_R^2}{4\kappa}\right)^2\right] + L_R\dfrac{dw}{dt} \\ \qquad \text{for} \quad w \le \dfrac{4\kappa L_R}{a_R^2}, \\ \dfrac{8v_B w L_R}{a_R^2} + L_R\dfrac{dw}{dt} \quad \text{for} \quad w > \dfrac{4\kappa L_R}{a_R^2}. \end{cases} \tag{7}$$

Equation (7) connects the pressure difference $(P_B - P_T)$ driving the flow with the vertical flow velocity w and the rate of variation of the flow velocity dw/dt.

Letting $L_R = L^*$ in equations (6) and (7) allows us to define a velocity scale $w^* = (4\kappa L_R)/a_R^2$, which in turn provides us with a Reynolds number:

$$Re \equiv \frac{w^*\rho a_R}{\mu} = \frac{4\kappa L_R\rho}{a_R\mu} = \frac{1}{Pr}\times\frac{4L_R}{a_R}, \tag{8}$$

where $Pr \equiv \nu/\kappa$ is the Prandt number (Delaney and Pollard, 1982).

Considering a basaltic magma with a viscosity $\mu \simeq 10^2$ Pa s and a density $\rho \simeq 3.10^3$ kg m^{-3}, and assuming that both the magma and the surrounding rocks have the same thermal diffusivity $\kappa = 10^{-6}$ m^2 s^{-1}, while $L_R \simeq 10^3$ m and $a_R \simeq 1$ m, the resulting Reynolds number is $\simeq 10^{-1}$, which is small compared to 1.

Such dimensional analysis is generally used to neglect the inertial term $\rho dw/dt$ in the momentum equation (1). Because of the nonlinearity in w that enters equation (7), $(P_B - P_T)$ as a function of w may not be single-valued when dw/dt vanishes. Contrary to the case of the viscosity being constant, in which a priori neglecting dw/dt is valid, here the inertial term has to be kept in the equation; as we will see below, it actually plays an important role in the dynamics of the phenomenon we are studying (Barenblatt, 1996, p. 10).

3.2. Two shallow magma reservoirs fed by a deeper source

Having described in section 3.1 the geometry of our model and the equations that govern the fluid flow between the shallow reservoirs, we now present the equations that govern the evolution of pressure inside the shallow chambers. As the magma is either flowing in or out of one of the two chambers, its volume changes. This change of volume ΔV in either chamber can easily be related to the change of overpressure ΔP inside the chamber by assuming that it is embedded in an elastic medium. In this case, the change of pressure is given by:

$$\Delta P = E\frac{\Delta V}{V}. \tag{9}$$

For an incompressible magma, the proportionality constant E depends on the intrinsic elastic properties of the surrounding rocks, as well as on the geometry of the chamber (e.g., Tait et al., 1989; Delaney and McTigue, 1994). We will refer to E as the effective bulk modulus of either magma chamber (Huppert and Woods, 2002).

The volumetric flux associated with the pipe of radius a_r is simply $w\pi a_r^2$. The volumetric flux feeding the shallow reservoirs from below is $Q_S = (a_S^4\pi/8\mu L_S)[P_S - P_B - \rho g L_S]$ (e.g., Lenglin et al., 2008; Pinel et al., 2010). With this additional information on the model parameters, we can finally write down the three coupled ordinary differential equations that govern the model:

$$\frac{dP_B}{dt} = \frac{a_S^4 E\pi}{V_B 8\mu L_S}[P_S - P_B - \rho g L_S] - w\frac{E\pi a_R^2}{V_B},$$

$$\frac{dP_T}{dt} = w\frac{\pi a_R^2 E}{V_T},$$

$$\frac{dw}{dt} = -\frac{8w}{a_R^2 L_R}\left[v_B L_R + \frac{\alpha\Delta T}{2L_R}\left(L_R - \frac{wa_R^2}{4\kappa}\right)^2\right]$$
$$\qquad + \frac{1}{\rho L_R}[P_B - P_T - \rho g L_R]. \tag{10}$$

The first equation relates the change of pressure P_B in the deeper shallow chamber with the influx coming from the underlying source region and the outflux leaving towards the shallower reservoir. The second equation relates the change of pressure P_T in the shallower chamber with the flux of magma arising from the chamber below. Finally, the third equation couples the variation of the vertical velocity w of the magma with the difference of pressure $(P_B - P_T)$ between the two shallow reservoirs.

By taking into account the fact that the pressure driving the flow is the sum of the lithostatic pressure at the outlet of the pipes and the overpressure of the magma reservoirs, i.e., $P = P_{litho} + \Delta P$, the former equations become:

$$\frac{dP_B}{dt} = \frac{a_S^4 E\pi}{V_B 8\mu L_S}[\Delta P_S - \Delta P_B + \Delta\rho g L_S] - w\frac{E\pi a_R^2}{V_B},$$

$$\frac{dP_T}{dt} = w\frac{\pi a_R^2 E}{V_T},$$

$$\frac{dw}{dt} = -\frac{8w}{a_R^2 L_R}\left[v_B L_R + \frac{\alpha\Delta T}{2L_R}\left(L_R - \frac{wa_R^2}{4\kappa}\right)^2\right]$$
$$\qquad + \frac{1}{\rho L_R}[\Delta P_B - \Delta P_T + \Delta\rho g L_R]. \tag{11}$$

Here $\Delta\rho = \rho_r - \rho$ is the density contrast between the surrounding rocks and the magma, while ΔP_S, ΔP_B, ΔP_T are the overpressures of the corresponding reservoirs. The system of equations (11) shows that the fluid flow in our model is driven by both the chamber overpressure and the buoyancy of the magma (Jaupart and Tait, 1990). If $\Delta\rho$ is kept constant, the buoyancy term acts as a constant flux and constitutes a constant forcing term.

3.3. Dimensional analysis

The dimensionless variables are denoted by primes, and they are defined by:

$$w = w'w^*, \quad w^* = \frac{4\kappa L_R}{a_R^2},$$

$$t = t'\frac{8\mu L_S V_B}{E\pi a_S^4},$$

$$P = P'\frac{L_R\rho 8v_B w^*}{a_R^2}. \tag{12}$$

The velocity scale w^*, mentioned in section 3.1 in connection with equation (8), is the velocity above which most of the heat still resides in the magma (Delaney and Pollard, 1982). The time scale in the second equation of (12) is the characteristic time associated with the balance of pressure between one shallow reservoir of volume V_B and a deep source region (e.g. Pinel et al., 2010). Finally, the pressure scale is a viscous pressure scale that can be extracted from the steady-state version of the momentum equation (1).

Table 1

List of main variables and parameters described in the main text.

Description	Symbols
Variables	
Pressure in the top magma chamber	P_T
Pressure in the bottom magma chamber	P_B
Overpressure in the top magma chamber	ΔP_T
Overpressure in the bottom magma chamber	ΔP_B
Horizontally averaged vertical velocity	w
Difference of overpressures	$X = \Delta P_T - \Delta P_B$
Volume concentration of crystals	β
Geometrical parameters	
Feeding conduit length	L_S
Shallow conduit length	L_R
Feeding conduit radius	a_S
Shallow conduit radius	a_R
Magma properties	
Dynamic viscosity	μ
Kinematic viscosity	ν
Density	ρ
Thermal diffusivity	κ
Density contrast	$\Delta \rho$
Critical volume concentration of crystals	$\beta_\star$
Crystal growth rate	χ
Number density of crystals	n
Rock properties	
Density	ρ_r
Shear modulus	G
Magma chambers properties	
Volume of the top magma chamber	V_T
Volume of the bottom magma chamber	V_B
Effective bulk modulus	E
Effective bulk modulus for compressible magma	$\bar{E}$
Important dimensionless parameters	
γ – proportional to the vertical acceleration dw/dt	$(\frac{8\nu_B}{a_R^2})^2 \frac{\rho D_R V_T}{E\pi a_R^2}$
A – proportional to the temperature difference ΔT	$\alpha \Delta T / \nu_B$
B – proportional to the length ratio L_S/L_R of the pipe segments	$a_R^4 L_S / a_S^4 L_R$
C – volume ratio between the two magma chambers	V_B/V_T
$\nu_\star$ – viscosity ratio	ν_T/ν_B

By substituting these dimensionless variables into the system (11), dropping the primes, and considering that $\Delta \rho = 0$, one ends up with the following dimensionless system:

$$\frac{d\Delta P_B}{dt} = \Delta P_S - \Delta P_B - w \frac{L_S a_R^4}{L_R a_S^4}, \tag{13a}$$

$$\frac{d\Delta P_T}{dt} = w \frac{V_B}{V_T} \frac{a_R^4 L_S}{a_S^4 L_R}, \tag{13b}$$

$$\frac{dw}{dt} = \gamma [f(w) + \Delta P_B - \Delta P_T], \tag{13c}$$

where

$$f(w) = \begin{cases} -w\left(1 + \dfrac{A}{2}(1-w)^2\right) & \text{for} \quad w \leq 1, \quad \text{and} \\ -w & \text{for} \quad w > 1. \end{cases} \tag{14}$$

Four dimensionless parameters appear in equation (13):

$$\gamma = \frac{8\nu_B}{a_S^2}^2 \frac{\rho L_S V_B}{E\pi a_R^2}, \quad A = \frac{\alpha \Delta T}{\nu_B}, \quad B = \frac{a_R^4 L_S}{a_S^4 L_R}, \quad C = \frac{V_B}{V_T}. \tag{15}$$

As described in the following subsection, the values of these four dimensionless parameters strongly affect the qualitative dynamics of the system. A complete listing of variables and parameters appears in Table 1.

3.4. Linear stability analysis and Hopf bifurcation

In order to understand the behavior of such a system and its relevance to the geodetic observations of deformation presented in section 2.2, we assume first that the dimensionless flux entering the deeper reservoir is constant, $Q \equiv \Delta P_S - \Delta P_B = \text{const}$. The number of variables of the resulting system can be reduced by letting $X \equiv \Delta P_T - \Delta P_B$, which leads to a system of two coupled differential equations that governs the evolution of the pressure difference X between the two magma chambers, and the vertical velocity w of the magma:

$$\frac{dX}{dt} = -Q + (1+C)Bw, \tag{16a}$$

$$\frac{dw}{dt} = \gamma(f(w) - X). \tag{16b}$$

System (16) has a unique fixed point, i.e., a single stationary solution that corresponds to $dX/dt = dw/dt = 0$. This fixed point (X_0, w_0) is given by:

$$X_0 = f(w_0), \tag{17a}$$

$$w_0(1+C) \cdot B = Q. \tag{17b}$$

The first step to understand the dynamics of such a nonlinear system is to linearize it around the fixed point (17), by letting ($X = X_0 + \epsilon\xi$, $w = w_0 + \epsilon\omega$), substituting into system (16), expanding in ϵ, and gathering terms that are of order one in ϵ. This procedure yields:

$$\begin{aligned} \frac{d\xi}{dt} &= (1+C)B\omega, \\ \frac{d\omega}{dt} &= \gamma\left(\left.\frac{df}{dw}\right|_{w_0}\omega - \xi\right). \end{aligned} \tag{18}$$

The eigenvalues of the linear system (18) are

$$\lambda_\pm = \frac{\gamma}{2}\left(\left.\frac{df}{dw}\right|_{w_0} \pm \left(\left.\frac{df}{dw}\right|_{w_0}^2 - \frac{4(C+1)B}{\gamma}\right)^{1/2}\right). \tag{19}$$

A nonlinear dynamical system is linearly unstable when at least one of the eigenvalues of its linearization (18) has a positive real part. The fixed point thus loses its stability when (df/dw) at $w = w_0$ becomes positive, since γ is always positive. In this case, any trajectory of the system starting near the fixed point will necessarily spiral away from it. One can show that this transition is possible only for values of the fixed point defined by the double inequality:

$$\frac{2}{3} - \frac{1}{3}\sqrt{1 - \frac{6}{A}} < w_0 < \frac{2}{3} + \frac{1}{3}\sqrt{1 - \frac{6}{A}}. \tag{20}$$

This inequality enables us to extract two criteria for the fixed point to be unstable. First, A must be larger than 6, otherwise (df/dw) cannot be positive at w_0. Second, equation (17a) and inequality (20) imply that the magma flux Q feeding the shallow reservoirs must verify the following two-sided inequality:

$$\left(\frac{2}{3} - \frac{1}{3}\sqrt{1 - \frac{6}{A}}\right)(1+C)B < Q < \left(\frac{2}{3} + \frac{1}{3}\sqrt{1 - \frac{6}{A}}\right)(1+C)B. \tag{21}$$

Far enough away from the fixed point, (df/dw) can change sign, as shown in Fig. 4, thus giving rise to a limit cycle, i.e. to
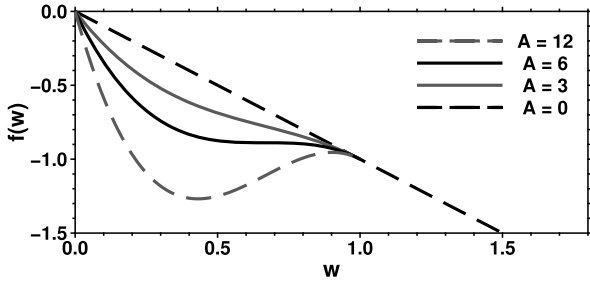
Fig. 4. Changes in the shape of $f(w)$ as the dimensionless parameter A varies. When $A \geq 6$, there is a range of w-values for which $f(w)$ increases. This increase is the critical characteristic of f that gives rise to the emergence of the relaxation oscillations.
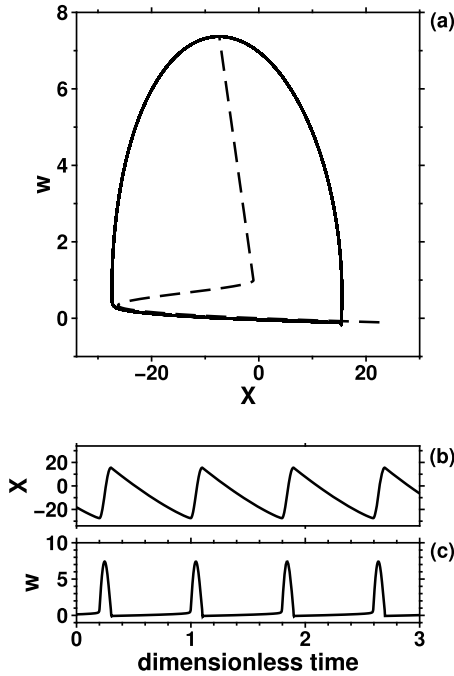

Fig. 5. Nonlinear oscillation of the reduced model governed by Eq. (16). (a) Phase portrait in the (X, w)-plane; (b) and (c) the associated time series representing, respectively, $X(t)$ and $w(t)$. All plots are computed using $(\gamma, A, B, C, Q) = (10, 350, 1, 200, 70)$ in the equations. In panel (a), the closed trajectory (heavy solid line) is the limit cycle, while the dashed curve represents the function $X = f(w)$ that allows one to understand the shape of the limit cycle. For $1/\gamma$ small — with $1/\gamma = 0.1$ here — the limit cycle follows, to a good approximation overall, either the graph of $X = f(w)$ or the two vertical lines on either side of this graph.

a closed, periodic trajectory that arises when the fixed point becomes unstable; see Fig. 5a. B. Van der Pol (Van der Pol, 1926) first described such oscillatory solutions and called them "relaxation oscillations." Their anharmonic, asymmetric shape arises from the nonlinearity of the damping term (Van der Pol, 1926; Guckenheimer and Holmes, 1983). In fact, the name itself was associated by Van der Pol with a much slower relaxation of a variable, after reaching a threshold value, so that the entire period of the oscillation is dominated by its relaxation time.

In the present case, the phase of increasing X is much shorter than the decreasing phase, thus leading to a sawtooth-shaped oscillatory time series, as shown in Fig. 5b. Another characteristic feature of relaxation oscillations is that their amplitude does not depend on the initial state from which they arise, but on the model parameters, contrary to classical harmonic oscillations of linear systems (Van der Pol, 1940).

The change in the dynamics of a nonlinear deterministic system from a unique stable fixed point to a stable closed orbit — like the

one seen in Fig. 5 — is called a Hopf bifurcation (Guckenheimer and Holmes, 1983; Ghil and Childress, 1987; Jordan and Smith, 2007).

4. Exponential inflations followed by oscillations

4.1. Two successive exponential inflations

The first aspect of Okmok dynamics that needs to be understood is the presence of two consecutive episodes of exponential inflation that have different characteristic time scales, called here τ_1 and τ_2 (Fig. 2a). A common explanation for the presence of exponential inflation is to consider a single shallow reservoir fed by a source region inside which pressure is constant (e.g., Pinel et al., 2010).

We assume first that the deeper one of the two shallow chambers in Fig. 3 is fed by a deep source and is not connected to any other reservoir. The evolution of ΔP_B can then be expressed analytically as:

$$\Delta P_B = \Delta P_B(0) \exp(-t/\tau_1) + \Delta P_S (1 - \exp(-t/\tau_1)), \qquad (22)$$

where $\tau_1 = V_B 8\mu L_S / E\pi a_S^4$. Here, the characteristic time scale τ_1 is related to the hydraulic connection between the source region and the shallow reservoir. This is also the time scale that was used to nondimensionalize the system of equations (11) in Section 3.3.

As shown in Fig. 2, the second exponential inflation phase occurred when the first one had almost subsided. This sequence of events suggests that the second inflation phase is related to the transfer of magma from the deeper chamber mentioned above to the shallower one of the two that are sketched in Fig. 3. Indeed, when the overpressure ΔP_B is large enough, then a new pathway for magma may open — or, as the case may be, an already existing one may reopen — allowing for the transfer of magma to a shallower reservoir.

If this scenario is correct, then the second exponential inflation phase can be related to the dynamics of pressure balance between the two shallow chambers. Neglecting, for now, that the bottom shallow reservoir is connected to a source region, it follows that ΔP_B and ΔP_T evolve according to:

$$\begin{aligned}
\Delta P_B &= \frac{V_T}{V_B + V_T}(\Delta P_B(0) - \Delta P_T(0))(1 - \exp(-t/\tau_2)) \\
&\quad + \Delta P_B(0), \\
\Delta P_T &= \frac{V_B}{V_B + V_T}(\Delta P_T(0) - \Delta P_T(0))(1 - \exp(-t/\tau_2)) \\
&\quad + \Delta P_T(0),
\end{aligned} \qquad (23)$$

where $\tau_2 = (8\mu D_R / E\pi a_R^4)(V_T V_B / (V_T + V_B))$ (Reverso et al., 2014).

If one assumes that E and μ are the same for both conduits and that $L_S a_R^4 / a_S^4 L_R \simeq 1$, then

$$\frac{\tau_1}{\tau_2} = \frac{V_T + V_B}{V_T}. \qquad (24)$$

This means that τ_1 is necessarily larger than τ_2 — as is the case for the fit to the Okmok time series in Fig. 2a — since $V_T + V_B \geq V_T$.

Clearly, the above heuristic reasoning is only acceptable to first order, and the entire system — i.e., the two reservoirs fed by a deep source region— should be treated as a whole, since the transfer of magma between the two shallow reservoirs affects the pressure of the bottom shallow reservoir, which in turn affects the flux of magma from the source region. The dynamics of this model — when neglecting the effect of temperature variations ΔT on the viscosity in the pipe — is governed by system (13) with $A = 0$.
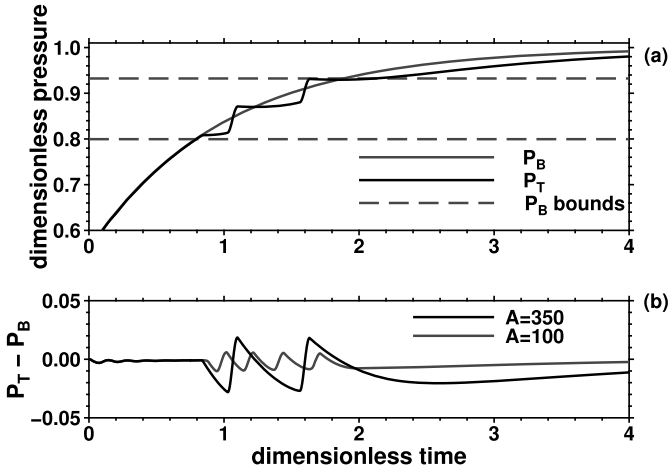
Fig. 6. Time series reflecting the dynamics of the reservoir overpressures ΔP_B and ΔP_T that are governed by the system (13). (a) Time series of both P_B (grey solid) and P_T (black solid); and (b) time series of $P_T - P_B$. The curves in (a) are computed using $(\gamma, A, B, C) = (10, 350, 1, 200)$, while the parameter values in plot (b) are the same, except that we add a time series computed also with $A = 100$. The bounds on ΔP_B (dashed) in panel (a) are given by the double inequality (25). Note also that the overpressures are normalized by the overpressure of the source region so that their values at equilibrium is 1.

The solution shows that, in fact, such a system does possess two characteristic time scales. One of them is larger than the τ_1 above and the other one larger than τ_2 but still smaller than τ_1 (see Appendix A).

4.2. Transition from exponential inflation to oscillations

The last phase of deformation at Okmok, prior to the 2008 eruption, started in 2004 when a damped oscillatory signal emerged from the second inflation phase (Fig. 2). Because of their relatively small amplitude the damped oscillations can only be observed on the GPS time series recorded at Okmok — such as the one shown in Fig. 2b — and not on the InSAR derived time series shown in Fig. 2a. This signal, as well as the transition from the exponential trend, can be explained using the system of differential equations (13).

As described above, the reduced system governed by equations (16)(a,b) behaves in an oscillatory manner only if the magma flux Q entering the system is bounded by the values given by the two-sided inequality (21); these values depend on the dimensionless parameters A, B, and C. This type of bounds on Q is also valid for the full system (13), even though in that case the flux Q is not constant and depends on the overpressure ΔP_B in the bottom chamber.

From the double inequality (21), one can derive the threshold values for ΔP_B required for the emergence of an oscillatory regime. The corresponding two-sided inequality for ΔP_B is given, in terms of the source overpressure ΔP_S, by

$$\Delta P_S - \left(\frac{2}{3} + \frac{1}{3}\sqrt{1 - \frac{6}{A}}\right)(1 + C)B < \Delta P_B < \Delta P_S$$

$$- \left(\frac{2}{3} - \frac{1}{3}\sqrt{1 - \frac{6}{A}}\right)(1 + C)B. \qquad (25)$$

Fig. 6 shows the time series of the overpressures ΔP_B and ΔP_T that are governed by equations (13). As the pressure equilibrates between the shallow reservoir and the source region, both ΔP_B and ΔP_T increase. When P_B reaches the lower threshold in inequality (25), the pressure starts to oscillate in a sawtooth manner, as illustrated in Fig. 6a. These oscillations are superimposed onto

the overall trend of exponential pressure increase and are slightly damped as the flux entering the shallow system decreases. When the pressure ΔP_B reaches the upper threshold of inequality (25) the oscillations cannot be sustained anymore.

This qualitative dynamics can be directly compared with the observations at Okmok. The fact that the observed oscillations are damped and start when the rate of inflation decreases suggests that the transition from the exponential inflation regime to the oscillatory one is controlled by the evolution of the flux entering the shallow system.

Note that, as shown in Fig. 6b, as the parameter A increases, both the amplitude and the period of the oscillations increase. Because the time in Fig. 6a is scaled by the characteristic time scale τ_1 associated with the pressure balance between a source region and a shallow reservoir, the period of the oscillations is also quantitatively consistent with observations at Okmok.

The model simulations plotted in Fig. 6 show that the amplitude of the dimensionless pressure oscillations is roughly equal to 0.1, when choosing $A = 350$. The pressure scale we used is $[P] = L_R \rho 8 \nu_B w^* / a_R^2$. Let us choose $L_R = 500$ m, $\rho = 3.10^3$ kg m^{-3}, $\nu_B = 10^2$ Pa s, $w^* = 0.004$ m s^{-1} and $a_R = 1$ m, so that $[P] \simeq 1$ MPa. The overpressure variations in the top chamber induced by the oscillations have then an amplitude $\simeq 0.1$ MPa. Since the oscillations represent $\simeq 10\%$ of the amplitude of the total deformation, this is consistent with the observed surface displacement and with overpressures that come into play during eruptions in general that is of order 1–10 MPa (Huppert and Woods, 2002).

Of course, all the parameters involved — such as A, a_R, and so on — can be tuned to produce oscillations of smaller or larger amplitude in order to produce deformations that would fit well the observed surface displacements.

This consistency between model results and observations is achieved by using large values for A — e.g., in Fig. 6a, $A = 350$ — which imply large variations in the viscosity as the magma is flowing from a reservoir to another. This point is further discussed in section 5.2.

5. Discussion

5.1. Volatile exsolution in the magma chamber

The GPS time series show that the oscillations at Okmok are damped (Fig. 2b). While part of the damping can be explained by the decreasing flux of magma supplying the system (section 4.2), an other contribution may come from exsolution of gas in the shallow magma chamber.

If volatiles are present in the magma and are exsolved, then the effective bulk modulus E of the magma chamber can change significantly (Huppert and Woods, 2002). Larsen et al. (2013) showed that water is present in melt inclusions entrapped at a depth of roughly 3 km and above, with H_2O concentration in the melt inclusions of the 2008 ejecta ranging from about 0.1% to about 4.4% of weight fraction. Although these estimates of H_2O content in the melt inclusions show that, in all likelihood, the water exsolves mainly during the decompression of the magma while ascending to the surface, some of it might also have exsolved in the shallow chamber while crystallization occurred; see Larsen et al. (2013, Fig. 11), and Tait et al. (1989, and the references therein).

Let us assume that only one volatile species, H_2O say, is present when the melt arrives in the deeper shallow reservoir, at a depth of about 2 km. We follow the formalism of Huppert and Woods (2002) to determine how the presence of the volatile affects the effective bulk modulus E of the magma chamber; see Appendix B for details on the model. The variation of E as a function of the weight fraction of crystals is shown in Fig. 7.
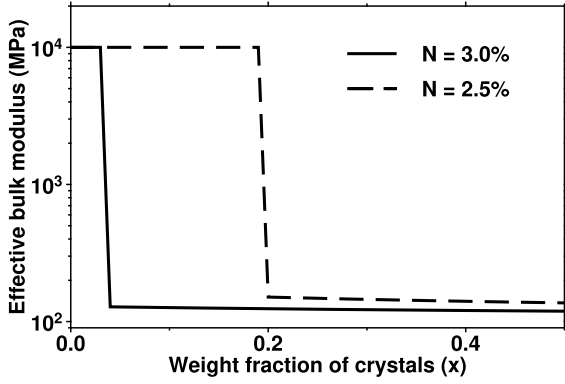
Fig. 7. The effective modulus E of a magma chamber as a function of both the weight fraction of crystals x and the total weight fraction of volatile. The computation is explained in Appendix B, and the curves are computed using $\rho_m = 3000 \ kg \ m^{-3}$, $\rho_c = 3200 \ kg \ m^{-3}$, $T = 1100 °C$, $P = 60$ MPa, and $E = 10^{10}$ Pa.
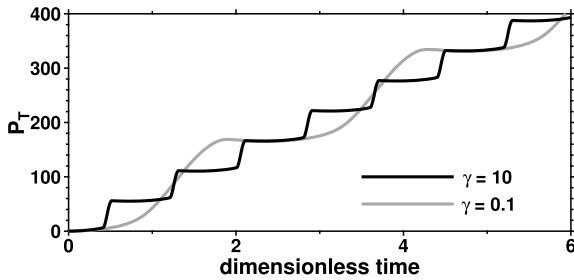

Fig. 8. Effect of volatile exsolution on the oscillations in the top magma chamber's overpressure ΔP_T. Two time series have been computed using two values of γ that are separated by two orders of magnitude: this is approximately the effect that volatile exsolution would have on γ, according to the results plotted in Fig. 7. Such an increase in γ causes, in turn, a decrease in the amplitude and period of the oscillations. Both time series have been computed using $(A, B, C, Q) = (350, 1, 200, 70)$.

We chose two values of total H_2O: $N = 2.5\%$ and $N = 3\%$ per weight; both are within the range measured in the melt inclusions at Okmok. In both cases, as crystallization develops the resulting melt can reach H_2O saturation. At this point, the effective bulk modulus values drop by almost two orders of magnitude, which leads to an increase in γ by about two orders of magnitude.

The pressure evolution of P_T in the case of a constant flux from the deep source region into the shallow chambers is shown in Fig. 8 for $\gamma = 0.1$ and $\gamma = 10$. Clearly, such a large change in the vertical acceleration of the magma leads to large changes in both the amplitude and period of the pressure oscillations inside the upper magma chamber.

5.2. Amplitude of the viscosity variations inside the conduit

In the model, the critical dimensionless parameter is $A = \alpha \Delta T / \nu_B$, which corresponds to the ratio between the viscosity variations induced by the vertical temperature gradient ΔT along the pipe and the viscosity ν_B at its bottom outlet. Nonlinear oscillations can take place only if $A \geq 6$, which means that the viscosity needs to increase by 600% or more during the magma ascent. Another important point is that the period and amplitude of the oscillations increases as A increases, as shown in Fig. 6b, where we used $A = 350$ (solid black) vs. $A = 100$ (solid grey) to illustrate this effect. In Fig. 6a, we used only $A = 350$ in order to simulate oscillations of large enough period and amplitude compared, respectively, with the time scale and the pressure variations that are associated with pressure equilibrium between the shallow chambers, on the one hand and the deep source region, on the other; see the discussion at the end of section 4.2.

Larsen et al. (2013) carried out a thermometric study based on the analysis of equilibrium between liquid, olivine microlite and olivine phenocryst in samples from the 2008 eruption, and obtained temperature estimates inside the Okmok plumbing system that are in the 1000–1200 °C range. According to these authors, olivine phenocryst and olivine microlite crystallized under different pressure conditions, suggesting that they formed at different depth. Their estimates lead us to suppose that the same temperature interval provides a plausible range for the vertical temperature gradient across the shallow plumbing system before the 2008 eruption, i.e., $\Delta T \simeq 200 °C$.

Inside the pipe, the temperature gradient is smaller and results from the competition between the advected heat and the conducted heat, cf. Eq. (3). According to the simple model presented above, if $L_R = 1$ km and $a_R = 1$ m, and we assume that the velocity $w = w^* = 0.004 \ m \ s^{-1}$, the amplitude of the vertical temperature variations inside the pipe would be $\simeq 100 °C$ when the surrounding temperature gradient is $\Delta T \simeq 200 °C$.

If one assumes, as in the model governed by equations (13)–(15), that viscosity varies only with the temperature, this corresponds to viscosity variations of approximately one order of magnitude, i.e., $A \simeq (10^3 - 10^2)/10^2 \simeq 9$; see, for instance, Shaw et al. (1968). According to the linear stability analysis in section 3.4, this viscosity variation suffices to give rise to oscillations, but their amplitude and period would not be large enough to produce ground deformations that are measurable using geodetic instruments.

Both decrease of temperature and release of H_2O-dominated fluids during magma ascent lead to crystallization and increase of viscosity (e.g., Shaw et al., 1968; Hess and Dingwell, 1996). These phenomena would increase sufficiently A to generate oscillations of easily measurable period and amplitude.

5.3. Oscillations due to decompression-induced crystallization

The key relation that leads to nonlinear oscillations in the model of section 3.1 is the coupling between the flow velocity and the viscosity. We considered so far that this coupling is achieved through the advected heat, cf. equation (3).

Other processes occurring in the conduit that are not linked to temperature variations may also induce a coupling between viscosity and velocity (e.g., Melnik and Sparks, 1999). We consider herewith the effect of H_2O degassing and the induced crystallization (Blundy and Cashman, 2001). As the magma rises from the bottom to the top reservoir, H_2O can exsolve as the result of its solubility decreasing with decreasing pressure. This process probably occurred in Okmok's plumbing system, as described by Larsen et al. (2013).

Here the associated crystallization kinetics provides a relation between the rate of decompression and the amount of crystals that, in turn, induces a coupling between velocity and viscosity because the viscosity is a function of crystal content in the magma (Lejeune and Richet, 1995; Caricchi et al., 2007).

To discuss the latter processes, we used the model developed by Barmin et al. (2002) that considers the dynamics of fluid flow inside a vertical conduit in which decompression of the magma induces crystallization. Following Barmin et al. (2002) and to focus on the cause of the oscillations in such a system, we make the following hypotheses: (1) there are no density changes due to gas exsolution and crystal growth; (2) the nucleation of crystals is instantaneous; (3) crystal growth rate is constant; and (4) the magma is a Newtonian liquid in which viscosity depends on volume concentration of crystals via a step function.

In the static case — i.e., the time derivatives dw/dt and $\partial \beta / \partial t$ are equal to zero — the vertical pressure gradient and vertical gradient of volume concentration of crystals are given by
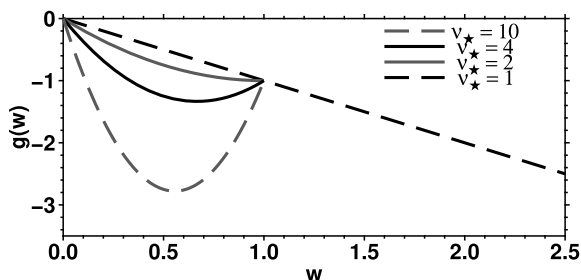
Fig. 9. Changes in the shape of $g(w)$ as the dimensionless parameter $\nu_\star$ varies. This figure is quite similar to Fig. 4 for the function $f(w)$. Here, when $\nu_\star \geq 2$, there is a range of w-values for which $g(w)$ increases. This increase is the critical characteristic of g that gives rise to the emergence of the relaxation oscillations.

$$\frac{1}{\rho}\frac{dP}{dz} = -\rho g - \frac{8\nu w}{a_R^2}; \quad \nu = \begin{cases} \nu_T, & \beta < \beta_\star, \\ \nu_B, & \beta \geq \beta_\star; \end{cases} \tag{26a}$$

$$w\frac{d\beta}{dz} = (36\pi n)^{1/3}\beta^{2/3}\chi. \tag{26b}$$

Here β is the volume concentration of crystals, $\beta_\star$ is a concentration threshold of crystals above which the viscosity changes from ν_B to ν_T, and χ is the linear growth rate of the crystals, while n is the number density of crystals and is taken to be constant. From the qualitative dynamics point of view, equation (26b) plays a role analogous to the heat equation (3) in the model of section 3.1, namely it introduces a coupling between the velocity and the crystal content that produces, in turn, a coupling between velocity and viscosity.

One can follow the same approach as in section 3.1. Equation (26b) yields the length scale,

$$L_\star = \frac{w\Delta\beta}{(36\pi n)^{1/3}\beta_\star^{2/3}\chi}, \tag{27}$$

above which the crystal content β is approximately greater than $\beta_\star$, where $\Delta\beta$ is the difference between the threshold value of crystal content $\beta_\star$ and the crystal content value at the bottom outlet of the conduit, i.e., $\Delta\beta = \beta_\star - \beta$ at $z = 0$. The length scale $L_\star$ is analogous to the length scale L^* of section 3.1.

Knowing $L_\star$, it is easy to integrate equation (26a) to obtain a relation that relates the pressure difference to velocity:

$$g(w) \equiv \Delta P_T - \Delta P_B = \begin{cases} -(1-\nu_\star)w^2 - \nu_\star w \\ \quad \text{for} \quad w \leq 1, \quad \text{and} \\ -w \quad \text{for} \quad w > 1. \end{cases} \tag{28}$$

This relation has been rendered dimensionless by using the viscous pressure scale of section 3.3 and the velocity scale

$$w_\star = \frac{(36\pi n_{ch})^{1/3}\beta_\star^{2/3}\chi L_R}{\Delta\beta} \tag{29}$$

obtained by letting $L_\star = L_R$. The key dimensionless parameter appearing here is $\nu_\star = \nu_T/\nu_B$; it is analogous to the parameter A in the model of section 3.1.

The shape of $g(w)$ is displayed in Fig. 9 and has to be compared directly with the shape of $f(w)$ displayed in Fig. 4. The two functions are similar: there is a range of velocities for which the derivative of either function changes sign. In other words, for a certain velocity range, the absolute value of the pressure difference $\Delta P_T - \Delta P_B$ increases as velocity decreases. This change of slope is possible only when $A > 6$ for $f(w)$ or when $\nu_\star > 2$ for $g(w)$. It is this change of sign that is responsible for the linear instability that gives rise to oscillatory behavior of the volcano's plumbing system in both cases.

We can also derive here two-sided bounds on the dimensionless flux feeding the system, namely

$$(1+C)B < Q < \frac{\nu_\star}{-2(1-\nu_\star)}(1+C)B \tag{30}$$

This analysis shows that the emergence of nonlinear oscillations is also possible when a highly nonlinear viscosity profile, for instance a step function, is present inside the conduit.

5.4. The sources of the deformation

Independent data sets suggest that the Okmok plumbing system is composed of several reservoirs and that two shallow storage zones played a role in the occurrence of the 2008 eruption; see section 2.1 and Freymueller and Kaufman (2010), Larsen et al. (2013). The two consecutive exponential inflations that had different time scales can also be interpreted as an evidence for interactions between two distinct shallow magma chambers (section 4.1).

The plumbing model we proposed in section 3 is designed to provide an explanation of the oscillatory dynamics of the Okmok volcanic system. This model is based on the evidence supporting the role of several reservoirs in the occurrence of the 2008 eruption; it is, however, not consistent with part of the geodetically based localization of the deformation source. Most authors seem to agree with the fact that the source of the deformations that occurred between 1997 and 2008 remained stable; see, for instance, Biggs et al. (2010) and the reference therein. Here we discuss this inconsistency.

An important point shown by the model of section 2.1 is that the oscillations occur once the pressure reaches an equilibrium between the top and the bottom chamber. Fig. 6 illustrates this result: while P_T is oscillating (black curve), P_B is inflating exponentially (grey curve) but it follows exactly the same trend as P_T. Hence, the resulting surface deformation might still reflect the deformation of the bottom reservoir and thus the inversions based on surface displacements may still localize the bottom reservoir.

This plausible inference implies that the time interval that is best suited to examine whether the deformation requires the presence of two reservoirs is the one that follows immediately after the end of the first exponential inflation and precedes the oscillations, i.e., roughly between the beginning and the middle of the year 2003. We may, therefore, expect to see a 'sombrero'-type of pattern indicative of shallow uplift superimposed over deeper subsidence during this interval, provided the coherence of the interferograms is good enough (Fialko and Pearse, 2012). However, the interferograms displayed in Lu et al. (2010) show that the interferograms' coherence is essentially limited in extent to the Okmok volcano's caldera, and is thus insufficient to draw conclusions about the wider presence or absence of such a pattern.

During the post-eruptive deformation, Freymueller and Kaufman (2010) detect a shallow uplift superimposed over a deeper subsidence, thanks to GPS data recorded at the station OKFG that is far from the rim of the caldera, at about 5 km; see again Fig. 1. InSAR data may, therefore, not be able to detect such a sombrero type of pattern because of the lack of coherence outside the caldera limits that is probably due to topographic and atmospheric effects inherent to InSAR analysis, effects that are difficult to correct for.

Fournier et al. (2009) carried out a numerical experiment in which the positions of a moving Mogi source were inverted using GPS data recorded at Okmok from 1997 to 2008. Their results show a shift in the horizontal localization of the source between the beginning and the middle of the year 2003 (Fournier et al., 2009, Fig. 7a). These authors disregarded the result so obtained, because a fixed Mogi source gave a better fit to the data than the moving one. Still, we feel that, given the limited data, one should

not rely exclusively on this fit in discriminating between a single- and a multiple-reservoir model, given all the arguments in favor of the latter.

Concerning the depth of the source of the deformation that occurs between 1997 and 2008, the GPS-based study of Fournier et al. (2009) found that it is located roughly 2.5 km below sea level. The joint inversions of Biggs et al. (2010) used both InSAR and campaign GPS data and found that the source is located slightly deeper, at about 3 km. These independent estimates of source depth suggest that the associated uncertainty is $\simeq 500$ m.

In addition, the GPS-based study of Freymueller and Kaufman (2010) suggests that the source of the co-eruptive deflation is roughly 500 m shallower than the same authors' estimation for the previous inflations. The two shallow reservoirs that played a role in Okmok's 2008 eruption may be separated by a conduit of length $L_R \simeq 500$ m, which lies within the uncertainty of the above depth estimates.

The relative proximity of the two shallow reservoirs may thus render the two indistinguishable from each other by the use of purely geodetic inversions. The above arguments, together with the intrinsic correlation between either volume or pressure change and source depth obtained using a Mogi model justify the apparent stability of the source from 1997 to 2008 reported by studies that relied exclusively on the latter.

6. Conclusion

Episodes of fast inflation, followed by longer quiet periods, are observed at the Okmok volcano, cf. Fig. 2. We have demonstrated that these sequences can be explained by the hydraulic interaction of two magma reservoirs connected by a conduit, as shown in Fig. 3, provided the viscosity varies with depth along this conduit. Several physical processes may contribute to such viscosity gradients in the melt; they include heat diffusion, fluid exsolution, and the formation of a solid phase as the magma crystallizes.

The simple model presented herein, and governed by equations (13)–(15), shows that a nonlinear oscillatory regime arises if: (i) the flux supplying the shallow reservoirs is limited within a specified, plausible range; and (ii) the viscosity gradient is sufficiently large. If these conditions are met, our model explains the observed deformation pulses as a manifestation of the internal variability of the magmatic system, without the necessity to call for ad hoc variations in external forcing.

The Okmok-type oscillations may not be unusual. Similar behavior was observed at Akutan volcano (Walwer et al., 2016; Ji et al., 2017). It would be interesting to test whether the model we propose applies to other active volcanic systems.

Acknowledgements

Appendix A. Nonoscillatory interaction of two shallow magma chambers fed by a deeper source

Let us consider the purely hydraulic, linear system (13) without any temperature-driven viscosity variation — i.e., with $A = 0$. In this case the system reduces to

$$\frac{d\Delta P_B}{dt} = \Delta P_S - \Delta P_B - B(\Delta P_B - \Delta P_T), \tag{31a}$$

$$\frac{d\Delta P_T}{dt} = BC(\Delta P_B - \Delta P_T); \tag{31b}$$

here B and C are the two dimensionless parameters introduced in equation (15); see Table 1.

The solution of the corresponding homogeneous system has necessarily the form

$$\begin{pmatrix} \Delta P_B \\ \Delta P_T \end{pmatrix} = \boldsymbol{\alpha} \begin{pmatrix} e^{\lambda_1 t} \\ e^{\lambda_2 t} \end{pmatrix}, \tag{32}$$

where $\boldsymbol{\alpha}$ is a constant matrix with entries that depend on the initial state. The exponents λ_1 and λ_2 are the eigenvalues of the matrix

$$\begin{pmatrix} -(1+B) & B \\ BC & -BC \end{pmatrix}, \tag{33}$$

and they are given by:

$$\lambda_1 = \frac{-(B(C+1)+1) + \left((B(C-1)-1)^2 + 4CB^2\right)^{1/2}}{2}, \tag{34a}$$

$$\lambda_2 = \frac{-(B(C+1)+1) - \left((B(C-1)-1)^2 + 4CB^2\right)^{1/2}}{2}. \tag{34b}$$

Because λ_1 and λ_2 are real, it follows that — in the absence of a viscosity gradient — the purely hydraulic system (31) cannot oscillate. Equations (34a) and (34b) also show that the dynamics of the system (31) is associated with two time scales, $(8\mu L_S V_B / E\pi a_S^4)(\lambda_1, \lambda_2)$.

Appendix B. Effect of a magma's volatile content on its bulk modulus

We follow Huppert and Woods (2002) to show how the presence of volatile can affect the effective bulk modulus E of the magma chambers. When the bulk density of the magma varies, mass conservation yields the equation

$$\frac{d}{dt}(\rho V) \equiv \rho \frac{dV}{dt} + V \frac{d\rho}{dt} = Q, \tag{35}$$

where $Q \gtrless 0$ is the total mass flux of magma either entering or leaving a chamber. The density ρ is a function of temperature, pressure, mass fraction of crystals and total mass fraction of volatile, either dissolved and exsolved.

Differentiating the equation (35) with respect to ρ gives the following equation

$$\frac{dV}{dt} + \frac{V}{\rho} \frac{\partial \rho}{\partial p} \frac{dp}{dt} = \frac{Q}{\rho} - \frac{V}{\rho} \frac{\partial \rho}{\partial T} \frac{dT}{dt}. \tag{36}$$

As we already saw in equation (9), volume change V inside the chamber can be related to pressure change P by

$$\frac{dV}{dt} = \frac{V}{E} \frac{dP}{dt}. \tag{37}$$

Substituting the above expression (37) into the equation (36) gives

$$V\left(\frac{1}{E} + \frac{1}{\rho} \frac{\partial \rho}{\partial P}\right) \frac{dP}{dt} = \frac{Q}{\rho} - \frac{V}{\rho} \frac{\partial \rho}{\partial T} \frac{dT}{dt}. \tag{38}$$

One can now identify the left-hand side of equation (38) with the right-hand side of equation (37) to define an effective bulk modulus $\overline{E}$ for a magma chamber with compressible magma by the following harmonic mean between E and $\rho \partial P / \partial \rho$:

$$\frac{1}{\overline{E}} = \frac{1}{E} + \frac{1}{\rho} \frac{\partial \rho}{\partial P}. \tag{39}$$

The harmonic mean plays an important role in calculating the effective properties of heterogeneous materials (e.g., Ericksen et al., 2012).

The effective modulus $\overline{E}$ for a magma chamber that contains volatile can be evaluated by using an expression of the bulk density ρ as a function of the pressure P, namely

$$\rho = \left(\frac{n}{\rho_g} + (1-n) \left(\frac{x}{\rho_c} + \frac{1-x}{\rho_m} \right) \right)^{-1}. \tag{40}$$

Here ρ_g and ρ_c are, respectively, the gas density and the crystal density, x is the weight fraction of crystals, and n is the weight fraction of exsolved volatile.

The gas density ρ_g obeys the ideal gas law

$$\rho_g = \frac{P}{RT}, \tag{41}$$

where R is the universal gas constant. The exsolved volatile content n is assumed to follow Henry's law. For water, this law states that $n = N - sP^{1/2}(1-x) \geq 0$ when the magma reaches saturation, and $n = 0$ otherwise. Here N is the total volatile content and $s = 4 \cdot 10^{-6} \text{ Pa}^{-1/2}$.

References

Barenblatt, G.I., 1996. Scaling, Self-Similarity, and Intermediate Asymptotics. Cambridge University Press.

Barmin, A., Melnik, O., Sparks, R., 2002. Periodic behavior in lava dome eruptions. Earth Planet. Sci. Lett. 199 (1–2), 173–184.

Biggs, J., Anthony, E.Y., Ebinger, C.J., 2009. Multiple inflation and deflation events at Kenyan volcanoes, East African Rift. Geology 37 (11), 979–982.

Biggs, J., Lu, Z., Fournier, T., Freymueller, J.T., 2010. Magma flux at Okmok Volcano, Alaska, from a joint inversion of continuous GPS, campaign GPS, and interferometric synthetic aperture radar. J. Geophys. Res. 115 (B12).

Blake, S., 1981. Volcanism and the dynamics of open magma chambers. Nature 289 (5800), 783–785.

Blundy, J., Cashman, K., 2001. Ascent-driven crystallisation of dacite magmas at mount st Helens, 1980–1986. Contrib. Mineral. Petrol. 140 (6), 631–650.

Bruce, P.M., Huppert, H.E., 1989. Thermal control of basaltic fissure eruptions. Nature 342 (6250), 665–667.

Caricchi, L., Biggs, J., Annen, C., Ebmeier, S., 2014. The influence of cooling, crystallisation and re-melting on the interpretation of geodetic signals in volcanic systems. Earth Planet. Sci. Lett. 388, 166–174.

Caricchi, L., Burlini, L., Ulmer, P., Gerya, T., Vassalli, M., Papale, P., 2007. Non-newtonian rheology of crystal-bearing magmas and implications for magma ascent dynamics. Earth Planet. Sci. Lett. 264 (3–4), 402–419.

Delaney, P., McTigue, D., 1994. Volume of magma accumulation or withdrawal estimated from surface uplift or subsidence, with application to the 1960 collapse of Kilauea volcano. Bull. Volcanol. 56 (6–7), 417–424.

Delaney, P.T., Pollard, D.D., 1982. Solidification of basaltic magma during flow in a dike. Am. J. Sci. 282 (6), 856–885.

Dvorak, J.J., Okamura, A.T., 1987. A hydraulic model to explain variations in summit tilt rate at Kilauea and Mauna Loa volcanoes. U.S. Geol. Surv. Prof. Pap. 1350 (2), 1281–1296.

Ericksen, J.L., Kinderlehrer, D., Kohn, R., Lions, J.L. (Eds.), 2012. Homogenization and Effective Moduli of Materials and Media, vol. 1. Springer Science & Business Media.

Fialko, Y., Pearse, J., 2012. Sombrero uplift above the altiplano-puna magma body: evidence of a ballooning mid-crustal diapir. Science 338 (6104), 250–252.

Fournier, T., Freymueller, J., Cervelli, P., 2009. Tracking magma volume recovery at Okmok volcano using GPS and an unscented Kalman filter. J. Geophys. Res. 114 (B2).

Freymueller, J.T., Kaufman, A.M., 2010. Changes in the magma system during the 2008 eruption of Okmok volcano, Alaska, based on GPS measurements. J. Geophys. Res. 115 (B12).

Ghil, M., Childress, S., 1987. Topics in Geophysical Fluid Dynamics: Atmospheric Dynamics, Dynamo Theory, and Climate Dynamics. Appl. Math. Sci., vol. 60. Springer Science & Business Media.

Guckenheimer, J., Holmes, P.J., 1983. Nonlinear Oscillations, Dynamical Systems, and Bifurcations of Vector Fields. Appl. Math. Sci., vol. 42. Springer Science & Business Media.

Hess, K., Dingwell, D., 1996. Viscosities of hydrous leucogranitic melts: a non-arrhenian model. Am. Mineral. 81 (9–10), 1297–1300.

Huppert, H.E., Woods, A.W., 2002. The role of volatiles in magma chamber dynamics. Nature 420 (6915), 493.

Jaupart, C., Mareschal, J.-C., 2010. Heat Generation and Transport in the Earth. Cambridge University Press.

Jaupart, C., Tait, S., 1990. Dynamics of eruptive phenomena. Rev. Mineral. Geochem. 24 (1), 213–238.

Ji, K.H., Yun, S.-H., Rim, H., 2017. Episodic inflation events at Akutan volcano, Alaska, during 2005–2017. Geophys. Res. Lett.

Jordan, D.W., Smith, P., 2007. Nonlinear Ordinary Differential Equations – an Introduction for Scientists and Engineers. Oxford University Press, Oxford, New York.

Larsen, J.F., Śliwiński, M.G., Nye, C., Cameron, C., Schaefer, J.R., 2013. The 2008 eruption of Okmok Volcano, Alaska: petrological and geochemical constraints on the subsurface magma plumbing system. J. Volcanol. Geotherm. Res. 264, 85–106.

Lejeune, A.-M., Richet, P., 1995. Rheology of crystal-bearing silicate melts: an experimental study at high viscosities. J. Geophys. Res., Solid Earth 100 (B3), 4215–4229.

Lenglin, O., Marsan, D., Got, J.-L., Pinel, V., Ferrazzini, V., Okubo, P.G., 2008. Seismicity and deformation induced by magma accumulation at three basaltic volcanoes. J. Geophys. Res. 113 (B12).

Lu, Z., Dzurisin, D., Biggs, J., Wicks, C., McNutt, S., 2010. Ground surface deformation patterns, magma supply, and magma storage at Okmok volcano, Alaska, from InSAR analysis: 1. Intereruption deformation, 1997–2008. J. Geophys. Res., Solid Earth 115 (B5).

Masterlark, T., Haney, M., Dickinson, H., Fournier, T., Searcy, C., 2010. Rheologic and structural controls on the deformation of Okmok volcano, Alaska: FEMs, InSAR, and ambient noise tomography. J. Geophys. Res., Solid Earth 115 (B2).

McTigue, D., 1987. Elastic stress and deformation near a finite spherical magma body: resolution of the point source paradox. J. Geophys. Res., Solid Earth 92 (B12), 12931–12940.

Melnik, O., Sparks, R., 1999. Nonlinear dynamics of lava dome extrusion. Nature 402 (6757), 37.

Mogi, K., 1958. Relations between the eruptions of various volcanoes and the deformations of the ground surfaces around them. Bull. Earthq. Res. Inst. 36, 99–134.

Peltier, A., Bachèlery, P., Staudacher, T., 2009. Magma transport and storage at piton de la fournaise (la réunion) between 1972 and 2007: a review of geophysical and geochemical data. J. Volcanol. Geotherm. Res. 184 (1), 93–108.

Pinel, V., Jaupart, C., Albino, F., 2010. On the relationship between cycles of eruptive activity and growth of a volcanic edifice. J. Volcanol. Geotherm. Res. 194 (4), 150–164.

Reverso, T., Vandemeulebrouck, J., Jouanne, F., Pinel, V., Villemin, T., Sturkell, E., Bascou, P., 2014. A two-magma chamber model as a source of deformation at Grímsvötn Volcano, Iceland. J. Geophys. Res., Solid Earth 119 (6), 4666–4683.

Shaw, H., Wright, T., Peck, D., Okamura, R., 1968. The viscosity of basaltic magma; an analysis of field measurements in Makaopuhi lava lake, Hawaii. Am. J. Sci. 266 (4), 225–264.

Tait, S., Jaupart, C., Vergniolle, S., 1989. Pressure, gas content and eruption periodicity of a shallow, crystallising magma chamber. Earth Planet. Sci. Lett. 92 (1), 107–123.

Van der Pol, B., 1926. On relaxation-oscillations. Philos. Mag. 2 (11), 978–992.

Van der Pol, B., 1940. Biological rhythms considered as relaxation oscillations. Acta Med. Scand., Suppl. 108, 76–87.

Walwer, D., Calais, E., Ghil, M., 2016. Data-adaptive detection of transient deformation in geodetic networks. J. Geophys. Res., Solid Earth 121 (3), 2129–2152.

Whitehead, J., Helfrich, K.R., 1991. Instability of flow with temperature-dependent viscosity: a model of magma dynamics. J. Geophys. Res., Solid Earth 96 (B3), 4145–4155.